Comparative study of the microstructure between a laser beam melted 17-4PH stainless steel and its conventional counterpart

N. Guennouni [a,b], A. Barroux [a,c], C. Grosjean [b], D. Maisonnette [b], E. Nivet [c], E. Andrieu [a], D. Poquillon [a], L. Laffont [a], C. Blanc [a,*]

[a] *CIRIMAT, Université de Toulouse, CNRS, INP-ENSIACET, 4 Allée Émile Monso, BP 44362, 31030, Toulouse cedex 4, France*
[b] *Pôle MMS, CETIM, 7 Rue de La Presse, 42000, Saint-Etienne, France*
[c] *Pôle MMS, CETIM, 74 Rue de La Jonelière, 44000, Nantes, France*

ARTICLE INFO

ABSTRACT

The aim of this work was to compare the microstructures of 17-4PH martensitic stainless steels (MSSs) obtained by conventional manufacturing (CM), and additive manufacturing (AM) using laser beam melting (LBM) process. Both materials were studied after the same H900 heat treatment. Significant differences in microstructure were observed between the two MSSs, with a higher austenite content for the AM-H900 sample, as compared to the CM-H900 sample. Transmission electron microscopy (TEM) analyses allowed to identify both retained and reversed austenite in the AM-H900 sample, but most part of the austenite detected was found to be reversed austenite. The high amount of reversed austenite in the AM-H900 sample was attributed to a heterogeneous distribution in austenite-stabilising elements in the solution heat treated AM sample, leading to a decrease in Ms value and subsequent increase in the driving force for the martensite to austenite transformation during the ageing at 480 °C. Moreover, TEM analyses highlighted thinner martensite laths for the AM-H900 steel as compared to the CM-H900 one. This was interpreted as an increase in both nucleation sites and growth rate for reversed austenite. Despite those differences in microstructure, the AM-H900 and CM-H900 samples showed similar tensile behaviour, with similar UTS and $Rp_{0.2}$ values, but a decrease in the strain to fracture was observed for the AM-H900 sample, probably related to the pores and/or to intergranular carbides.

Author statement

N. Guennouni: Investigations. Formal analysis. Validation. Visualization. Methodology. Data curation. Writing-original draft. Writing-Review&Editing, A. Barroux: Investigations. Formal analysis. Validation. Visualization. Methodology. Data curation. Writing-Review&Editing, C. Grosjean: Funding acquisition (financial support). Resources (Materials). Project administration. Supervision. Writing-Review&Editing, D. Maisonnette: Funding acquisition (financial support). Resources (Materials). Project administration. Supervision. Writing-Review&Editing, E. Nivet: Funding acquisition (financial support). Resources (Materials). Project administration. Supervision. Writing-Review&Editing, E. Andrieu: Conceptualization. Writing-Review&Editing, D. Poquillon: Methodology. Supervision. Validation. Conceptualization. Data curation. Writing-Review&Editing, L. Laffont: Investigations (TEM analysis). Methodology (for TEM analysis). Formal analysis (for TEM analysis). Writing-Review&Editing, C. Blanc: Funding acquisition. Methodology. Project administration. Supervision. Validation. Conceptualization. Data curation. Writing-original draft. Writing-Review&Editing.

1. Introduction

Precipitation-hardened (PH) stainless steels constitute a major improvement of stainless steels used so far in the first third of the 20th century. Among the PH steel, the 17-4PH martensitic stainless steel (MSS) is widely used in a large variety of applications, going from biomedical utensils to large turbine blades. As an established engineering alloy, 17-4PH MSS is a good candidate for additive manufacturing (AM). This new process has aroused widespread interest

because it brings up new ways to design parts, to optimise their shape and volume and thus to decrease their weight, as compared to conventionally manufactured (CM) parts. Moreover, despite the powder cost, the possibility to produce near-net shape parts allows an efficient and controlled-cost industrial production. However, a major issue is to evaluate the AM processes capability to reproduce microstructures similar to those obtained by conventional metallurgy, and then similar in-service properties.

Recently, abundant literature has shown that AM processes raise new challenges, in particular concerning the microstructure of the built parts; in this framework, 17-4PH MSS has been extensively studied. First, numerous data provided insight into 17-4PH MSS microstructure and its dependence on build orientation [1–7]. This is particularly true for as-built parts characterised by a strong anisotropy in the grain morphology and texture [8–15]. Post-building heat treatments were found to homogenise the microstructure, e.g. by eliminating the dendritic solidification structure and crystallographic texture [8,10], but other issues remain. Indeed, for 17-4PH MSS as well as for all other materials, microstructural defects, e.g. gas pores or lack-of-fusion pores, can be observed in AM materials [8,13,16–19]. Literature clearly showed that the total porosity and density of defects depend on numerous parameters, e.g. powder choice and process parameters [2,8, 13,18,20]. Hu et al. studied the influence of various machine parameters, i.e. scan velocity or slice thickness, on the amount of pores and defects of components built with 17-4PH powder [2]. They showed, on the basis of Vickers microhardness measurements, a decrease in samples hardness when the scanning velocity or slice thickness increased, in relation with the amount of pores and defects. The existence of those specific defects constitutes a major issue concerning the possibility to produce, by using AM processes, microstructures similar to those obtained by conventional metallurgy; nevertheless, these defects can be mitigated by optimizing the powder choice and process parameters [8].

Another critical issue is the capability to obtain with AM processes morphology, distribution and proportion of phases similar to conventional metallurgy. Literature clearly showed that conventional metallurgy led to a martensitic microstructure for 17-4PH MSS, hardened by the formation of Cu-rich precipitates after a heat treatment [8,10]. Most heat treatments developed start with an annealing step at 1040 °C, leading to a homogeneous distribution of atomic Cu in the Fe matrix [21]. One of the above optimised ageing treatments followed the annealing step: 482 °C for 1 h (H900), 566 °C for 4 h (H1050) or 621 °C for 4 h (H1150). Hsiao et al. [22] compared results from Vickers hardness measurements performed for 17–4PH MSS after these 3 ageing treatments. They showed that the H900 state led to the highest Vickers hardness, at around 440 HV, as compared to 370 HV and 300 HV after a H1050 and H1150 ageing, respectively. However, significant differences in the nature and distribution of phases are observed with AM processes as compared to conventional metallurgy. Alnajjar et al. showed that, for specific processing parameters, the as-built parts of 17-4PH MSS did not show a martensitic microstructure, but a ferritic one [23,24]. Other authors showed that martensitic microstructures were obtained after AM processes, but the built parts contained a non-negligible amount of austenite, before as well as after a heat treatment; furthermore, comparison of the data from the literature [6,8–13,25,26] showed that the austenite to martensite ratio varied in a very large range up to 100%.

A significant influence of the chemical composition and microstructure of the powder used, and of the nature of the vector gas used during the AM process, was evidenced on the resulting microstructure of 17–4PH MSS samples [4,6,15,26–28]. In particular, Murr et al. [6] highlighted that mostly martensitic microstructures were observed for the built parts when the AM process was performed under Ar, independently of the powder; when N_2 was used during the building process, mostly austenitic microstructures were obtained for N_2-atomised powder, i.e. austenitic powder, whereas for Ar-atomised powder, i. e. mostly martensitic powder, martensitic microstructures were obtained.

Furthermore, many literature data can be found concerning the influence of post-processing heat treatments on the microstructure of AM 17-4PH MSS, and different hypotheses are proposed to explain the differences in microstructure between CM and AM 17-4PH MSS [4,6,10,28, 29]. Among those data, the work of Wang et al. [26] can be cited: the authors explained the differences in microstructure and mechanical properties between AM and CM samples by considering the distribution of austenitic phase stabilisers, i.e. N and Ni in both MSSs. However, as clearly shown by Sun et al. [8], it is currently unclear how AM processes and post-processing heat treatments affect the microstructure of 17–4PH MSS. There are so many parameters that differ from a study to another that it is very difficult to propose relevant conclusions about the microstructures observed for AM parts. In that respect, it remains fundamental to share experimental results on this topic, giving the experimental details required. This will serve as part of a development of a "database" within the literature that will be likely to be used by other authors as well as industrials to help in the development of AM materials.

Therefore, the main purpose of the current study was to compare the microstructures of CM and AM 17-4PH MSS samples, both materials being subjected to the same heat treatment, i.e. H900 heat treatment (solution heat treatment followed by ageing). The microstructures were analysed at different scales, by using X-ray diffraction (XRD), optical microscopy (OM) and transmission electron microscopy (TEM). Some mechanical tests were performed to go further in the comparison of CM and AM 17-4PH MSS. The results were discussed with reference to earlier works of the literature reported for the same MSS. In order to provide input to the discussion and better explain the apparent discrepancies observed, attention was also paid to the microstructures of the powder used for the AM process, and those of the AM and CM samples before the H900 heat treatment, i.e. as-built AM samples and as-received CM samples.

2. Experimental procedure

2.1. Materials and specimen preparation

2.1.1. 17-4PH powder

The 17-4PH powder had been elaborated by Erasteel by atomisation under N_2 gas. It had been used previously 7 times, but it had never been mixed with other powders. Its chemical composition was determined by Plasma Emission Spectrometry on a Spectro ARCOS apparatus. Results are given in Table 1 showing that, despite the large number of recycling, the chemical composition of the powder remained in an accepted range for all solutes even if the amount of Si was in the upper range.

Table 1

Chemical composition (in wt. %) of the CM and AM samples. The chemical composition of the powder used for the AM process is also given. For comparison, the nominal composition of the 17–4PH steel (X5CrNiCuNb16-4 alloy) is reported (* AMETEK Spectrolab, ** Spectro ARCOS).

	C	Mn	Si	S	P	Ni	Cr	Mo	Cu	Nb	N	Fe
17-4PH . CM sample*	**0.036 ±** 0.002	**0.39 ±** 0.01	**0.35 ±** 0.02	**≤** **0.005**	**0.016 ±** 0.003	**4.49 ±** 0.11	**15.42 ±** 0.19	**0.15 ±** 0.01	**3.24 ±** 0.10	**0.26 ±** 0.02	**0.030 ±** 0.006	**Bal.**
17-4PH powder R7**	**0.037 ±** 0.003	**0.35 ±** 0.01	**0.64 ±** 0.05	**≤** **0.006**	**≤ 0.006**	**3.95 ±** 0.07	**16.14 ±** 0.17	**≤ 0.020**	**3.67 ±** **0.11**	**0.27 ±** 0.01	**0.0295** ±0.0002	**Bal.**
17-4PH AM sample R7*	**0.028 ±** 0.002	**0.32 ±** 0.01	**0.71 ±** 0.03	**≤** **0.005**	**0.007 ±** 0.002	**4.08 ±** 0.10	**16.20 ±** 0.19	**≤ 0.020**	**3.56 ±** 0.11	**0.27 ±** 0.02	**0.035 ±** 0.007	**Bal.**
X5CrNiCuNb16-4 alloy (NF EN 10088)	≤0.07	≤1.50	≤0.70	≤0.015	≤0.040	3.0 – 5.0	15.0 – 17.0	≤0.60	3.0 – 5.0	0.19 – 0.45	–	Bal.

2.1.2. AM, i.e. laser beam melted samples

All AM samples were built with the same set of parameters, by using the same 17-4PH powder (described in 2.1.1) and the same laser beam melting machine, i.e. an EOS DMLS M290 featuring a 400 W laser. During the process, the building plate was maintained at 200 °C. Ar was used as inert gas during the AM process, and a ceramic blade recoater maintained a constant 40-μm layer thickness. For this study, $100 \times 15 \times 70$ mm^3 parallelepipeds were built with the building direction corresponding to the 70-mm side (Fig. 1). The laser strategy implied a 67-degree rotation between each layer, and corresponded to a chessboard building. The hatching distance was 110 μm. Cubic samples were extracted from those parallelepipeds to study the microstructure in the three planes, i.e. XY (perpendicular to the building direction), XZ and YZ (both parallel to the building direction), of the AM samples (Fig. 1). For brevity reasons, only the results obtained for XY plane are detailed in the following, but similar results were obtained for the XZ and YZ planes. Cylinders were also removed from the parallelepipedic parts in order to machine tensile test specimens. The chemical composition of AM bulk samples was determined by Optical Emission Spectrometry with an AMETEK Spectrolab apparatus. Results are displayed in Table 1.

2.1.3. CM, i.e. wrought samples

CM 17-4PH MSS was provided as a 50-mm diameter wrought cylinder in H1025 metallurgical state (solution heat treatment at 1040 °C for 30 min followed by an ageing at 550 °C for 4 h). Cubes and cylinders were extracted from the bulk material for microstructure characterisation and mechanical tests, respectively. In the present work, for brevity reasons, only the microstructure data obtained for the plane perpendicular to the rolling direction are presented; a study of the other plane showed that the microstructure was isotropic. The chemical composition of the CM samples was determined as previously described for AM samples and is given in Table 1.

2.1.4. H900 heat treatment

Some of the as-built AM samples and of the as-received CM samples were subjected to a H900 heat treatment. Samples were placed inside a quartz-made cylindrical container under vacuum (10^{-5} mbar). Then, an argon flow was maintained to ensure an inert atmosphere during the two steps of the heat treatment. AM and CM samples in their container were first annealed for 30 min in a furnace previously set at 1040 °C, then cooled down to room temperature under air. Finally, the samples were heated from room temperature to 480 °C with a heating rate of 5 °C/
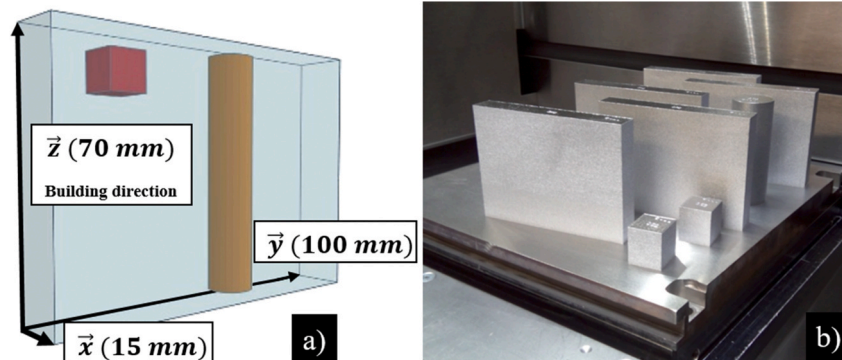

Fig. 1. a) 3D representation of the AM parts built for the study. The building direction during the AM process is indicated. Cubic samples and cylinders were removed from those parts to study the microstructure and the mechanical properties of the AM parts, respectively. b) picture of the building plate with the built parts.

min, maintained at 480 °C for 1 h, and air-cooled to room temperature.

2.2. Experimental methods and techniques

2.2.1. Characterisation of the microstructure

For all samples (CM and AM samples, and AM powder), the metallurgical phases were identified by using both XRD and energy-dispersive XRD analyses (EDXRD). Before performing the analyses, CM and AM samples were polished using P1200 SiC paper grade. For energy-dispersive XRD analyses, both samples were then electropolished in order to remove the strain-hardened zone generated by SiC paper where strain-induced austenite-to-martensite transformation was likely to occur. For XRD analyses, a Brucker D8 GIXRD machine was used with a Cu anticathode, set at 40 kV and 40 mA, characterised by a monochromatic X-Ray with a wavelength of 1.5418 Å. A θ-θ scan was performed from 40° to 120° with an angular step of 0.04° and an acquisition time of 2 s per angular step. A Lynxeye XE-T in 0D and high-resolution mode detector was used for the analysis; it was equipped with a built-in fluorescence filter, needed because of the natural Fe-fluorescence with Cu-radiation. Energy-dispersive XRD analyses were performed on a machine developed internally by the CETIM. A W anticathode was used and emitted a polychromatic white X-Ray beam with energies ranging from 12 keV to 40 keV. The energy-dispersive detector was fixed at a θ angle of 18.25°. In this setup, a maximum of 15 reflections for martensite phase and 18 reflections for austenite phase could be detected, with reduced peak overlapping as compared to XRD. The analysis of austenite content was done through iterative peak simulations. Finally, for a better understanding of the microstructures observed after the H900 heat treatment, additional XRD analyses were performed for both AM and CM samples to determine experimentally the Ms values after the solution heat treatment at 1040 °C. XRD analyses were performed with a Bruker D8 Advance equipped with a Cu anticathode set at 40 kV, a fast linear detector Vantec and an Anton Paar heating chamber. As-built AM samples and as-received CM samples were heated under a protective argon flux at 1040 °C for 30 min in the machine, then cooled down to room temperature under argon flux: XRD-diffractograms were acquired during the cooling with a 10 °C step, in the [700–40] ° C temperature range.

Further characterisation of the microstructure of CM and AM samples (distribution of the metallurgical phases and determination of the grain size) was carried out using an Axiover A1m Zeiss optical microscope (OM). Before the observations, the samples were first embedded using a carbon-rich epoxy resin with a Mecapress 3 hot mounting machine. Then, they were abraded using SiC paper until P2400 grade, and mirror-polished using diamond polishing pastes from the 6 µm grit to 0.25 µm grit on a manual Tegrapol 25 polishing machine. Finally, the samples were chemically etched. Fry reagent (1.5 g of cupric chloride, 30 mL of hydrochloric acid, 95 mL of water and 30 mL of ethyl alcohol) and Villela reagent (95 mL of ethyl alcohol, 5 mL of hydrochloric acid and 1 g of picric acid) were used to reveal the grain structure with former austenite grain boundaries and the martensite laths, respectively. The intercept technique was used to determine the average grain size for both AM and CM samples in agreement with ASTM E112 [30]. For each sample, three lines of a known length were drawn and the number of interceptions was counted. The same procedure was repeated after a rotation of the sample of 90°. In order to ensure the repeatability of the measurements, this procedure was applied at least on three different OM images and in the three directions (XY, XZ and YZ) for AM samples. Some scanning electron microscope (SEM) observations with a FEI Quanta450 machine equipped with an energy-dispersive spectrometer (EDS) Bruker Quantax (SDD) detector were also performed and EDS maps were plotted to study the distribution of the alloying elements.

The details of the microstructure of CM and AM samples were characterised by using TEM and scanning TEM (STEM). Slices with a thickness of about 500 µm were cut, then mechanically ground down to about 30 µm and finally electropolished by using a Tenupol-5 unit polisher with a 70% ethanol, 20% 2-butoxyethanol, 10% perchloric acid solution under 14 V at 2 °C. TEM imaging was performed using a JEOL JEM 2100 F operating at 200 kV and equipped with an EDS analyser (Brucker SDD Xflash 5030). Diffraction patterns were recorded using selected area electron diffraction (SAED) mode with a 150 nm aperture. STEM imaging in bright field (BF) and high angle annular dark field (HAADF) mode was performed using a JEOL cold-FEG JEM-ARM200F operated at 200 kV equipped with a probe Cs corrector (resolution 0.78 Å) and a JEOL CENTURIO SDD EDS detector (UMS Castaing, Toulouse, France).

Concerning the AM powder, the particle size distribution was determined by using a Mastersizer 3000 laser granulometer combined with a Mastersizer software. SEM observations were also performed to better characterise the microstructure of the AM powder, by using the FEI Quanta450 SEM previously mentioned. Before observation, the powder was embedded in a carbon-rich epoxy resin that made SEM observations more comfortable by avoiding electron-charging phenomena. Then, the sample was abraded and polished as previously described. Finally, it was slightly polished with an OPS finishing solution.

2.2.2. Mechanical tests

Mechanical tests, i.e. hardness measurements and tensile tests, were performed for both AM and CM samples in order to complete the characterisation of the microstructures and identify some possible changes in mechanical behaviour between AM and CM samples. Macro-hardness was measured by using a Vickers Frank GMBH 532 durometer with a 20-kgf load and a minimum of 9 measurements per sample. These measurements were completed by Vickers micro-hardness measurements using a Tukon 1202 durometer with a 0.1-kgf load. Results are obtained by calculating an average value from a 24-indent matrix for XY plane of AM samples, and a 90-indent matrix for CM samples and XZ/YZ planes of AM samples.

Tensile tests were carried out using a MTS Insight machine equipped with a 30 kN force cell with a strain rate of 10^{-3} s^{-1}. Cylindrical specimens with a 4-mm diameter and 30-mm long reduced section oriented in the z direction for AM samples were machined. Before the tests, all the specimens were carefully polished down to 0.25 µm grit diamond paste. During the tensile tests at room temperature, the strain was recorded using a contact extensometer with a gauge length of 25 mm. Specific attention was paid to the Young modulus values because they could be a good indicator of an excessive porosity for the AM MSS. Each tensile test therefore included a first load, at the nominal strain rate (i.e., 10^{-3} s^{-1}) and stopped at 600 MPa (far before the yield stress), then an unloading step at the same strain rate down to 100 MPa, and finally a final loading step until fracture. For all tests carried out, fracture occurred inside the extensometer gauge length. In agreement with ASTM E111 – 04, the Young modulus was evaluated by analysing the stress versus strain curve during the first unloading to limit the effects of micro-plasticity as unloading allows access to reversible elastic deformation. To ensure the reproducibility of the results, at least three tests were carried out for each specimen. At the end of each test, the necking was analysed all along the gauge length by measuring the tensile specimen diameter at different distances from the fracture surface using a Keyence CV-H500C camera with an HR F2/35 mm objective lens and 5 MP resolution, connected to a CV-X170FP controller. Fracture surfaces were observed by using a FEI Quanta450 SEM.

3. Results

3.1. Particle size distribution and microstructure of the 17-4PH powder

Fig. 2 shows the powder particle size distribution obtained by laser granulometry. Results highlight a bimodal character of the powder. D_n10, D_n50 and D_n90 values are equal to 4.3 µm (20.6), 7.6 µm (40.1) and 28.2 µm (69.2) considering density in number (in volume) of
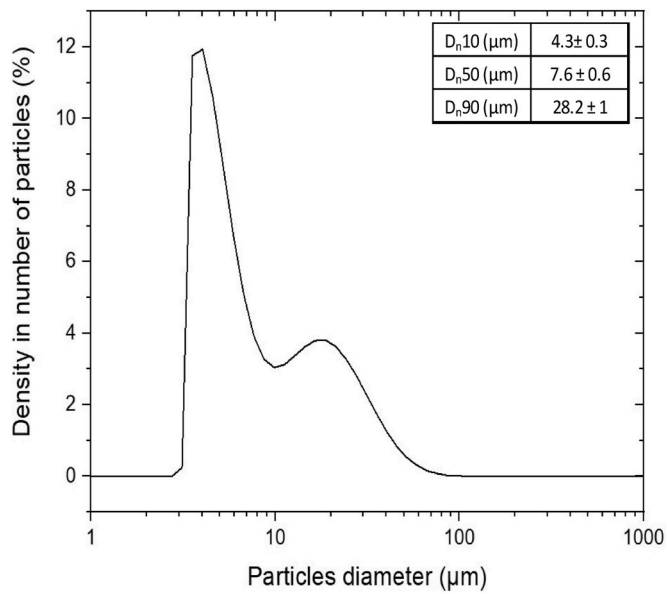
Fig. 2. Powder particle size distribution obtained by laser granulometry for the 17-4PH powder. (Black and white figure; single column).

particles, respectively. SEM images of the powder showed spherical particles for most of the grains (Fig. 3a). However, some smaller powder grains were observed to be partially melted to bigger particles, as already reported by several authors [20,27,31].

A noticeable contrast was observed for all powder grains in SEM image using backscattered electron (*BSE*) detector (Fig. 3b) contrary to what was observed with the secondary electron (*SE*) detector. This suggested a heterogeneous distribution of the alloying elements within the powder grains. EDS maps were plotted for a small surface area of a powder grain (cross-section view), depicted as a white rectangle in Fig. 3b. Fe, Cu, Nb and Ni EDS maps are shown in Fig. 3c, d, e and f, respectively. White areas observed in *BSE* mode seemed to correspond to areas depleted in Fe and enriched mainly in Cu and Nb; a slight Ni enrichment was also noticed in those areas. On the contrary, a homogeneous distribution of Cr (not shown) was observed. Taking into account the ability of alloying elements to stabilise one particular metallurgical phase, e.g. Ni for austenite, such a distribution could indicate the presence of both austenite and martensite in the powder grains. Therefore, the chemical heterogeneities observed in BSE image (Fig. 3b) suggested the presence of austenitic phase, even though it was not possible, with such an observation, to make a direct correlation between zones enriched with a specific element and the identification of an austenitic grain. The result should be in agreement with recent work done by Meredith et al. [28] who observed a small proportion of austenite for a N_2-atomised powder, and with work done by Zapico et al. who showed that the austenite content of the powder increased with the number of cycles [27].

3.2. Porosity and grain structure of the bulk samples

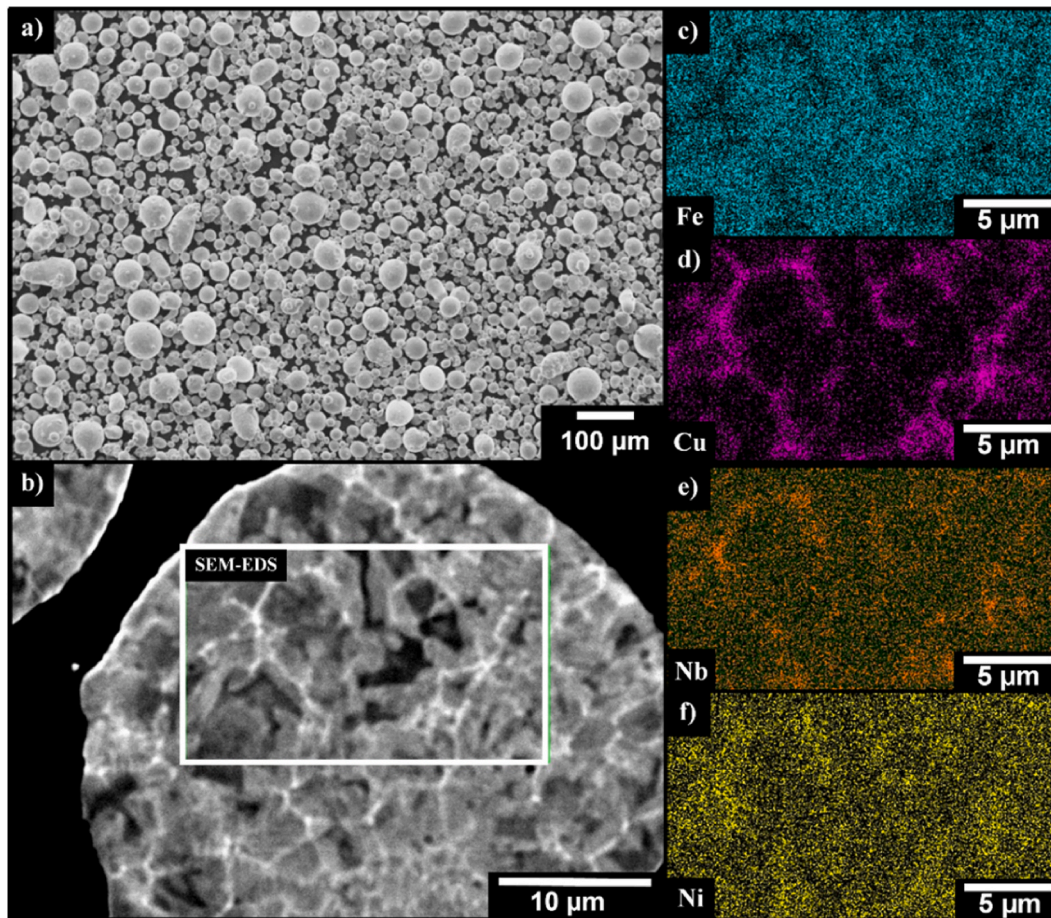Preliminary OM studies of polished samples prior to etching (not

Fig. 3. SEM images of the 17-4PH powder used in the AM process. a) secondary electron image of the powder grain morphology; b) chemical contrast detected in a powder grain using the backscattered electron detector; EDS maps obtained at 15 keV for a 10-mm working distance for Fe (c), Cu (d), Nb (e) and Ni (f) of the white square represented in Fig. b.
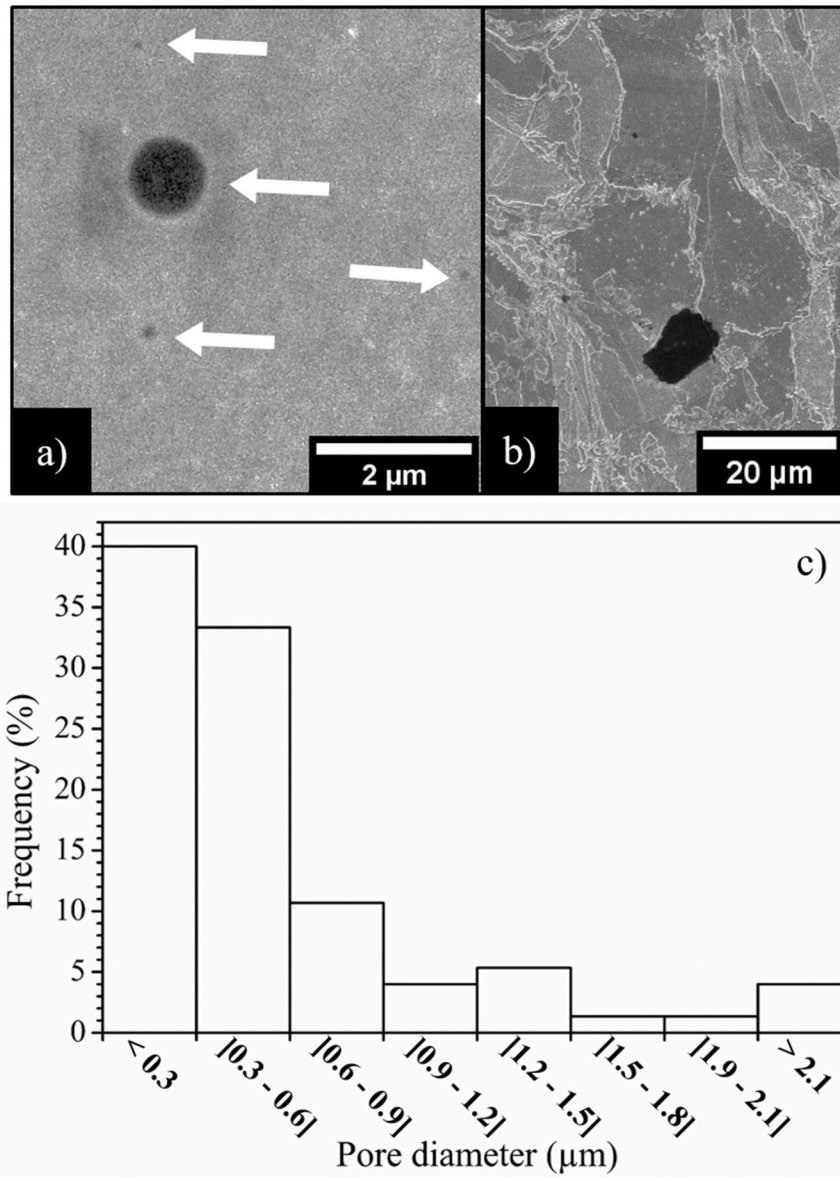
Fig. 4. SEM images of a) gas pores (the white arrows show the pores), and b) lack-of-fusion pores. c) gas pores diameter distribution obtained by analysing 25 SEM images. (Color on line only; two-columns).

shown here) allowed some defects to be observed in the as-built AM samples (Fig. 4). Most of those defects were either lack-of-fusion pores (less than 10 μm, Fig. 4b) or spherical pores (around 1 μm, Fig. 4a) caused by entrapped gas during the melting building process [8,13, 16–19].

In the current study, due to an appropriate choice of processing parameters, only a very small number of those defects was detected. It was particularly true for lack-of-fusion pores, with only 1 or 2 lack-of-fusion pores detected per sample, so that it was not relevant to plot a distribution in size of those defects. For the spherical pores, Fig. 4a was chosen because it shows the diversity of pores in terms of size. However, the distribution in size plotted in Fig. 4c clearly shows that most pores have a diameter of less than 1 μm. Hydrostatic weighting analysis of the AM samples gave an average volumetric mass of 7.71 g cm^{-3}. Using this value, the porosity rate has been calculated and is only 0.04%, in agreement with values obtained by analysing SEM images (results not shown).The same value was measured after H900 heat treatment.

OM observations of the samples after etching were performed for both materials in the different characteristic planes. The as-built AM sample was characterised by a strong anisotropy of the grain morphology, with grains elongated along the building direction (Fig. 5a), whereas large size cell-like grains (Fig. 5b) were observed in the plane perpendicular to the building direction (XY plane) with an average equivalent diameter between 70 and 90 μm; those grains were surrounded by much smaller grains, some with an average equivalent diameter less than 2 μm. This particular microstructure has already been reported in the literature [8,14,15,23]. For the as-received CM samples (Fig. 6a), a martensitic microstructure was observed with average grain diameter around 12 μm in both planes (perpendicular and parallel to the rolling direction). The H900 heat treatment (solution heat treatment followed by an ageing) allowed to homogenise the microstructure of the AM samples, so that there was no more evidence of the scan pattern on the microstructure, i.e. melt pools, or laser passes after H900 heat treatment: this homogenisation occurred during the first step of the H900 heat treatment, i.e. during the solution heat treatment at 1040 °C [8–10]. Therefore, results are only given for XY plane for AM samples. For CM samples, as no anisotropy of the microstructure was observed, only images of the plane perpendicular to the rolling direction were
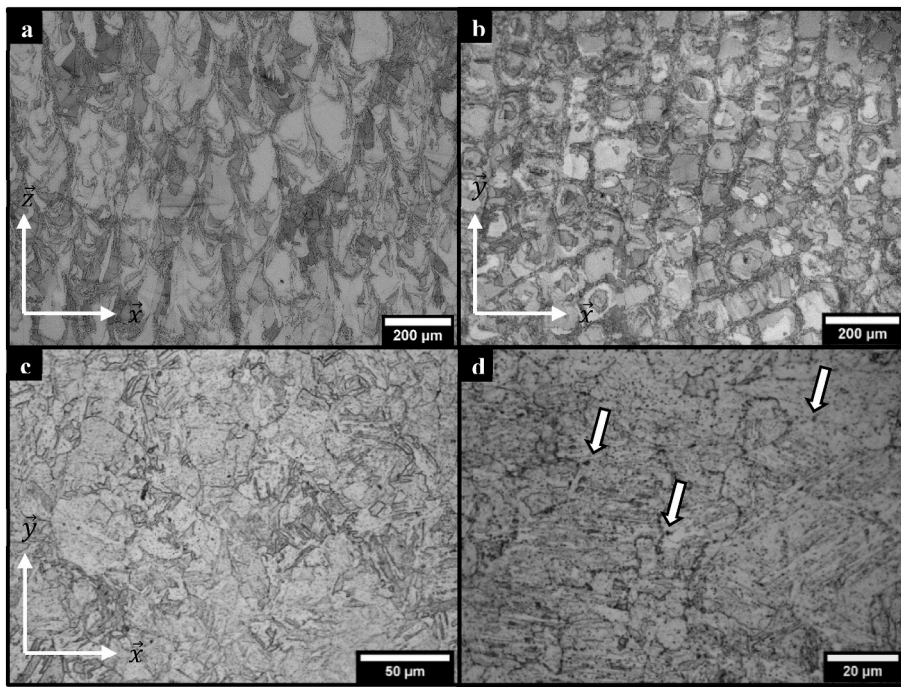
Fig. 5. OM images of the a) as-built AM (XZ plane), b) as-built AM (XY plane), c) and d) AM-H900 (XY plane) samples after chemical etching revealing former austenite grain boundaries and martensite lath packets. A low magnification was used for a) and b) in order to show the pattern resulting from the AM process. d) OM image of the AM-H900 sample at higher magnification to show intergranular NbC carbides (in black, white arrows). Observed contrast could be related to orientation contrast and/or chemical contrast after the etching. (Color online only; two-columns).
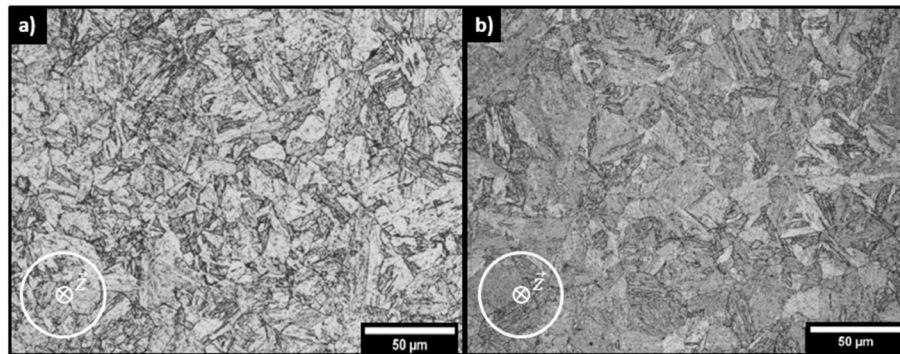

Fig. 6. OM images of the a) as-received CM (H1025) and b) CM-H900 samples after chemical etching revealing former austenite grain boundaries and martensite lath packets. Observed contrast could be related to orientation contrast and/or chemical contrast after the etching. Both micrographs correspond to a plane perpendicular to the rolling direction. (Color online only; two-columns).

given. A martensitic microstructure, with lath packets, was clearly observed for AM-H900 sample (Fig. 5c), but also for CM-H900 sample (Fig. 6b). The average equivalent grain diameter was around 13 ± 3 μm for AM-H900 samples and 14 ± 2 μm for CM-H900 samples. Those grain size values determined from OM images were confirmed by EBSD analyses (not detailed here). Numerous precipitates identified as carbides and mainly present at the grain boundaries were evidenced for AM-H900 samples (Fig. 5d). EBSD characterisations (not shown here) also confirmed that AM-H900 and CM-H900 samples exhibited no specific texture contrary to as-built AM samples, in good agreement with literature data.

Furthermore, to better understand the influence of the H900 heat treatment, additional SEM observations using a BSE detector were performed for the AM sample after the solution heat-treatment at 1040 °C for 30 min following the building process (Fig. 7a). Results showed chemical heterogeneities even though previous OM observations of AM-H900 samples (Fig. 5 c and d) suggested that the solution heat treatment had allowed a complete homogenisation of the microstructure for AM samples. Cu and Ni EDS maps (Fig. 7b and c, respectively) showed a heterogeneous distribution of both Cu and Ni in the samples: Ni was

clearly found to segregate in the interdendritic regions.

3.3. Phase analysis using X-Ray Diffraction for both powder and bulk samples

In order to provide a more accurate identification of the phases and quantitative data for both AM and CM samples (as-built AM/as-received CM and both AM and CM H900 samples) as well as for AM powder, X-Ray diffraction analyses were performed. Except for the AM as-built sample, all XRD patterns suggested that the grains were randomly oriented as previously indicated by referring to EBSD analyses, and in agreement with literature [8,10]. Results are given in Fig. 8. To facilitate the comparison, the diffractograms were normalised by the height of the peak of highest intensity, i.e. the martensite (α') (110) peak. First, results showed that austenitic peaks could be observed for the 17-4PH powder as suggested by Fig. 3, but the powder contained mainly martensite. Then, for all the bulk samples, both martensitic and austenitic peaks were also observed, except for the CM-H900 sample for which no austenitic peak was observed. For more clarity, Fig. 8 includes an insert with an enlarged representation to a narrower 2θ range, centred on the
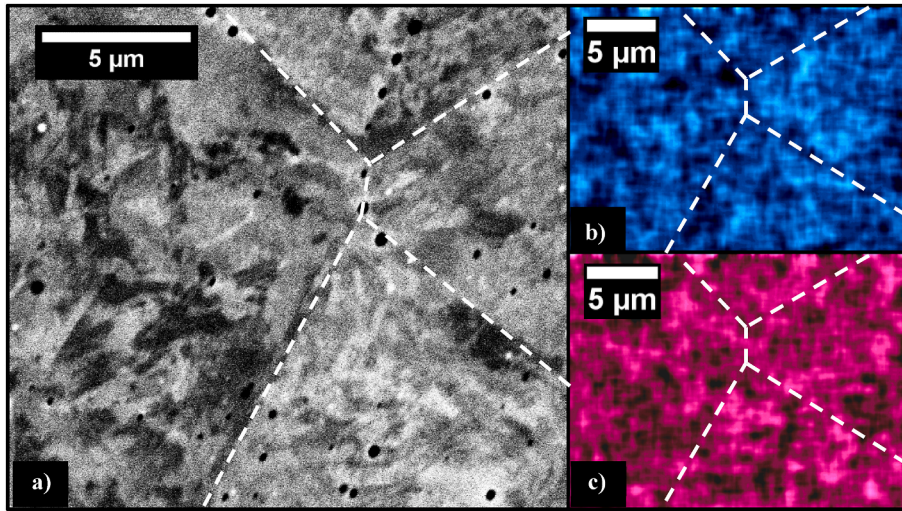
Fig. 7. a) SEM image (BSE detector) of the AM sample solution heat treated at 1040 °C for 30 min after the building process. EDS maps for b) Cu and c) Ni. Grain boundaries are represented with dashed lines.
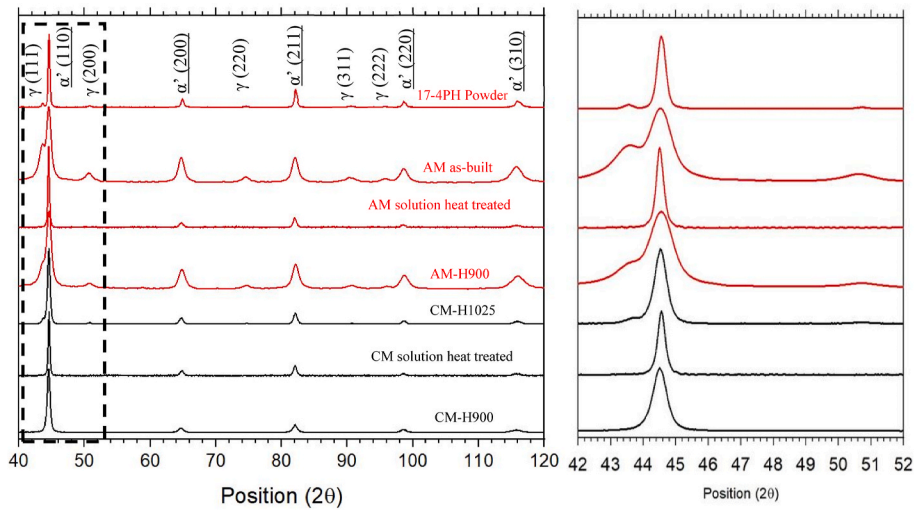
Fig. 8. Experimental X-ray diffractograms obtained with a Cu anticathode for the 17-4PH powder used to build AM samples, the as-built AM sample, the AM-H900 sample, the CM-H900 sample and the as-received (H1025) CM sample. Diffractograms are also given for solution heat treated AM and CM samples. A zoom was done on the black dashed rectangle in order to highlight the α′ (110), γ(111) and γ(200) peaks.
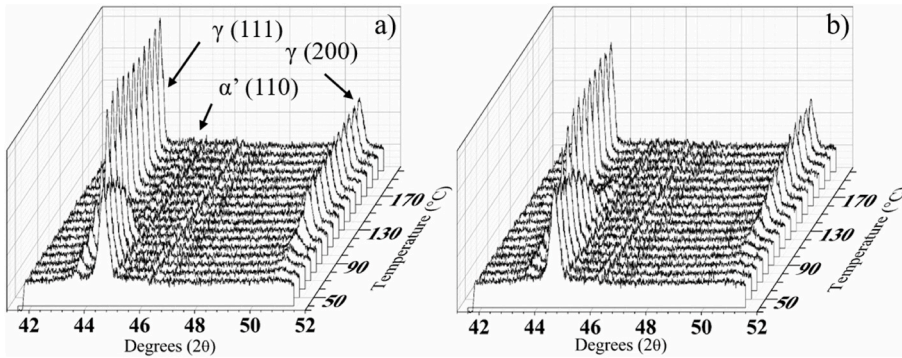
Fig. 9. XRD-diffractograms acquired during cooling from 1040 °C to room temperature, after a solution heat treatment at 1040 °C for 30 min for a) AM and b) CM samples. Only the XRD patterns acquired for temperatures lower than 200 °C are shown here for more clarity. (Black and white figure; two columns).

Fig. 10. TEM bright field images of martensitic laths for a) the CM-H900 sample and b) the AM-H900 sample showing a significant difference in the lath size. Inserts in Figs. a) and b) correspond to selected area electron diffraction patterns obtained with a 150 nm aperture in the [012] zone axis. (Color online only; two-columns).

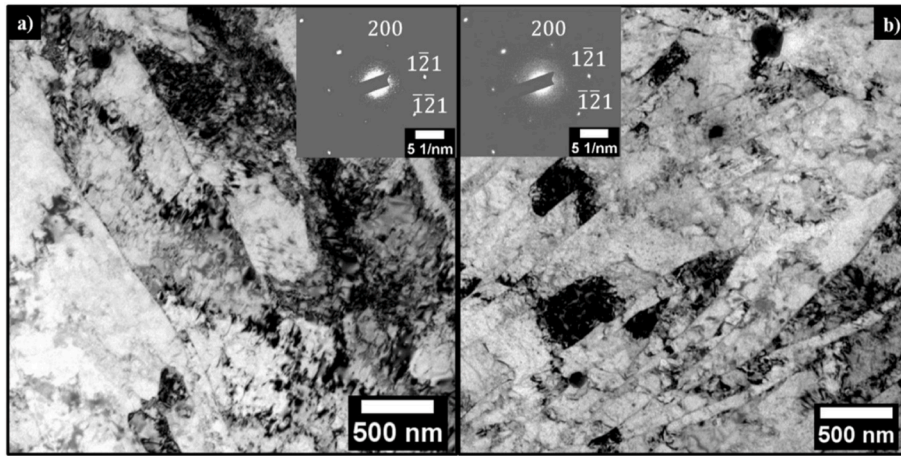martensitic (110) peak and the austenitic (111) and (200) peaks. Comparison of the diffractograms obtained for the 17-4PH powder, the as-built AM and the AM-H900 samples showed that the intensity of the main austenitic (111) peak increased from the powder to the bulk AM samples. Moreover, comparison between the AM-H900 and CM-H900 X-ray diffractograms showed that the austenitic (111) peak was intense for the AM-H900 sample, whereas no austenitic peak was observed for the CM-H900 sample.

To confirm these qualitative observations, the samples were analysed by using dispersive energy XRD, this technique allowing to separate more accurately the austenitic (111) peak from the martensitic (110) peak, and thus to determine more accurately the austenite content (Rietveld Refinement conducted on simulated XRD patterns with an iterative procedure). Results showed significant differences in austenite content between the AM samples and the CM samples, with values equal to $12.5 \pm 0.3\%$, $12.6 \pm 0.3\%$, $2.5 \pm 0.2\%$ and $0.8 \pm 0.2\%$ for the as-built AM, AM-H900, CM-H1025 and CM-H900 samples, respectively. These

values were in agreement with the qualitative analysis. Therefore, the results clearly showed that, although both AM and CM MSSs were subjected to the same heat treatment, i.e. H900 heat treatment, they were not in the same microstructural state, with significant differences in the austenite/martensite ratio. As a key point of this study is the different austenite/martensite ratio between AM and CM samples, it is of interest to remind that two forms of austenite could be formed, i.e. retained and reversed austenite. However they could not be distinguished using XRD analysis. It could be noted here also that no austenite was observed in X-ray diffractograms for both CM and AM samples, for the solution heat treated samples, i.e. after the sole heat treatment at 1040 °C followed by air cooling (Fig. 8). Considering the sensibility of the technique, this should not mean that austenite was definitively absent from the samples, but, it could be concluded that the amount of austenite in both the CM and AM samples after the heat treatment at 1040 °C was very low.

Then, for a better understanding of the microstructures observed
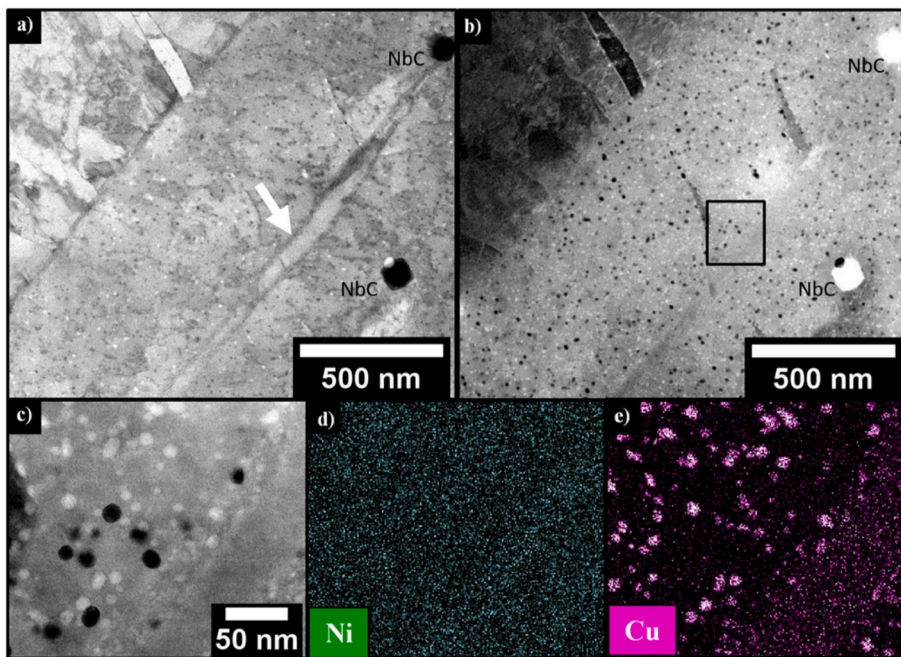

Fig. 11. STEM Bright Field (BF) a) and HAADF b) images of Cu-rich precipitates in martensitic laths and a retained austenite grain between 2 martensite laths (white arrow) for the AM-H900 sample. Precipitates appear in dark grey in BF mode and in white in HAADF mode. A higher magnification STEM HAADF image c) of the dark square in Fig. b) combined with the EDS maps of Ni d) and Cu e).
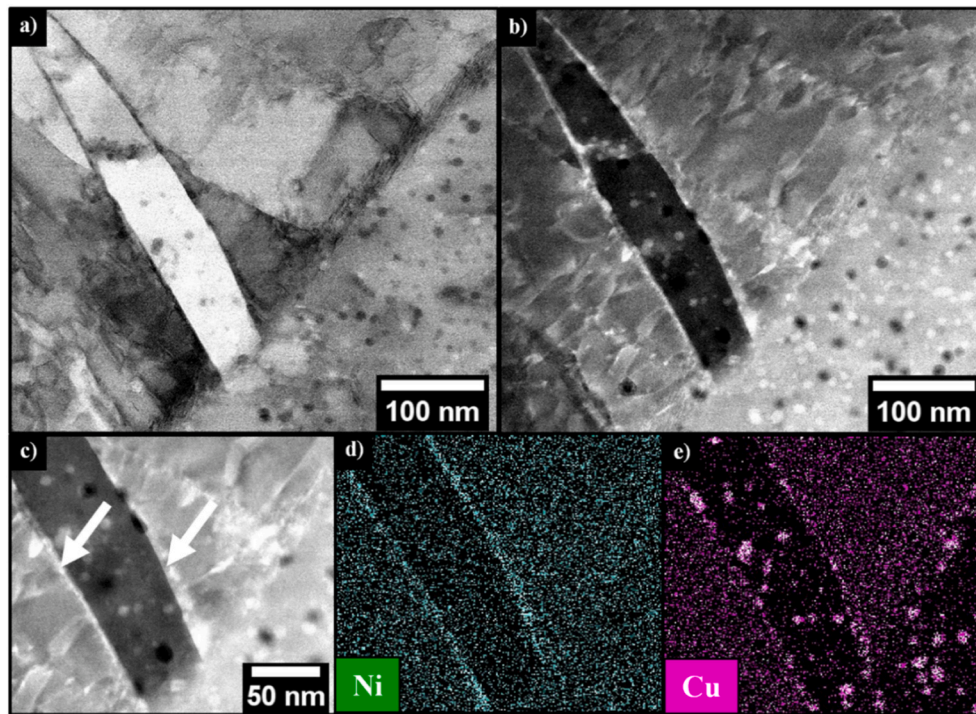
Fig. 12. STEM BF a) and HAADF b) images of Cu-rich precipitates in martensite laths for the AM-H900 sample. It can be noticed that some zones of the martensite laths do not contain Cu-rich precipitates. STEM EDS maps were plotted in the zone shown in c). Ni and Cu maps are shown in d) and e), respectively. Ni map allows a thin layer of reversed austenite to be evidenced all along a martensite lath.

after the H900 heat treatment, the Ms values after a solution heat treatment at 1040 °C for 30 min were determined for both the AM and CM samples, by acquiring XRD-diffractograms during the cooling from 1040 °C to room temperature. For more clarity, Fig. 9 shows only XRD-diffractograms in the [50–190] °C temperature range. Results clearly showed that martensitic peaks were detected when the temperature drops below 100 °C for AM sample but earlier, i.e. at 150 °C for CM sample. Taking into account the sensibility of XRD, the Ms values after a solution heat treatment at 1040 °C were about 100 °C and 150 °C for AM and CM samples, respectively.

3.4. TEM study of the bulk samples

To go further in the description of the microstructure of the 17–4PH MSSs, TEM and STEM studies were then performed for both CM-H900 and AM-H900 samples. Fig. 10 shows TEM bright field images of martensite laths for both CM-H900 and AM-H900 MSSs. Selected electron diffraction patterns performed for both MSSs showed an identical crystal structure, i.e. a *bcc* structure with a lattice parameter a ≈ 2.868 Å and a Im$\overline{3}$m space group characteristic of the martensitic phase. Based on the TEM observations, the apparent average width of martensite laths in CM-H900 samples varied from 700 nm to 2.5 μm, whereas the laths were thinner (from 50 nm to 800 nm) for AM-H900 samples.

STEM was also used to investigate the presence of austenite in the 17-4PH samples. An elongated zone characterised by a specific contrast (indicated by the white arrow in Fig. 11a) was observed between two martensite laths for the AM-H900 sample. SAED patterns obtained in this area (not shown here) revealed a *fcc* crystal structure (a ≈ 3.59 Å and Fm$\overline{3}$m space group) characteristic of the austenitic phase. This corroborated the presence of austenite in the AM-H900 sample, also shown by XRD analysis (Fig. 8). However, as previously reminded, austenite could correspond to either retained or reversed austenite. Considering that reversed austenite should be enriched with austenite-stabilising alloying elements, e.g. Ni [32], STEM EDS maps of Ni were plotted to differentiate between those two austenite phases. The black

Table 2
Macro- and micro-hardness of the as-built AM sample, as-received CM sample and AM/CM-H900 samples.

		$\overline{Hv_{20}}$	σ	$\overline{Hv_{0\,1}}$	σ
AM-as built	AM-as built XY	355	3	349	14
	AM-as built XZ	342	2	330	13
	AM-as built YZ	345	2	335	11
AM-H900	AM-H900 XY	386	4	353	17
	AM-H900 XZ	379	3	346	18
	AM-H900 YZ	381	4	344	23
CM-H1025		378	3	372	2
CM-H900		396	3	387	3

square in Fig. 11b shows the zone where the STEM EDS analysis was performed. This zone includes both some austenite and the adjacent martensite laths. A focus of that zone is illustrated in Fig. 10c. STEM EDS Ni map plotted for this zone (Fig. 11d) showed that no significant contrast could be observed regarding Ni, which showed a homogeneous Ni distribution of this element inside the sample. Therefore, it was assumed that this austenite grain corresponded probably to retained austenite that had not transformed into martensite during the quench step following the solution heat treatment at 1040 °C. The size of retained austenite grains was about a few tens of nanometers.

However, austenite was identified in other sites and with another morphology during STEM observations of the AM-H900 sample. Fig. 12 a, b and c show the presence of thin layers with specific contrast all along a martensite lath and on both sides of the lath (white arrows in Fig. 12c): these layers were identified as austenite using electron diffraction. STEM EDS analysis showed a strong Ni enrichment (Fig. 12d) in these thin layers as compared to the adjacent martensite laths, leading us to assume that these layers corresponded to reversed austenite. Based on those STEM analyses, reversed austenite grains had a width of a few nanometers.

Finally, it was of major importance to note that austenite was not observed in CM-H900 samples. However, considering the size of the
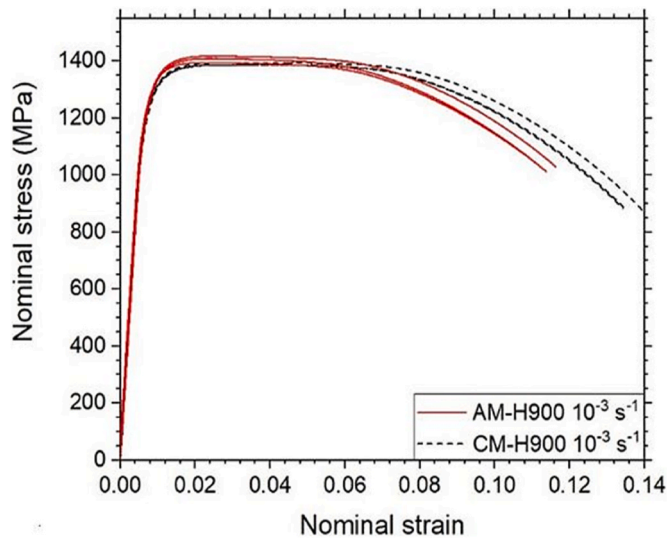
Fig. 13. Tensile curves plotted for both AM-H900 and CM-H900 samples in air, at room temperature and with an imposed strain rate of 10^{-3} s^{-1}. Tests were performed until fracture of the specimen. The first stage of the test including the first unloading is never visible because the corresponding plot is under the second and final loading.

Table 3

Main mechanical properties determined from tensile curves along z axis for both AM-H900 and CM-H900 samples. ε_i ε_f and σ_R are defined in the text.

Sample	E (GPa)	UTS (MPa)	$Rp_{0.2}$ (MPa)	ε_i	ε_f	$\Delta\varepsilon$ ε_{f-} ε_i	σ_R (MPa)
CM-1	201	1387	1243	0.030	0.956	0.926	2244
CM-2	201	1394	1256	0.033	0.966	0.933	2273
CM-3	201	1387	1253	0.035	0.941	0.906	2228
AM-1	202	1408	1278	0.023	0.68	0.657	1941
AM-2	204	1395	1295	0.022	0.668	0.646	1930
AM-3	204	1417	1293	0.025	0.636	0.611	1937

zone analysed by TEM, it was necessary to remind that the presence of austenite in CM samples could not be neglected. That said, such a result was consistent with previous XRD analyses, showing a very low amount of austenite in CM-H900 as compared to AM-H900 sample (Fig. 8).

STEM observations also allowed Cu-rich precipitates to be observed for both CM-H900 and AM-H900 samples. However, comparison of STEM images at low magnification for both CM-H900 and AM-H900 samples clearly showed a difference in Cu-precipitates size and distribution between the two samples. Concerning CM-H900 samples, only a few Cu-rich precipitates were observed. On the contrary, numerous Cu-

rich precipitates with an average diameter ranging from 10 to 15 nm were observed for the AM-H900 sample on STEM bright field and HAADF images (Figs. 11 and 12). They were clearly visible in dark grey in BF mode and in white in HAADF mode (Fig. 11a and b). Moreover, the STEM EDS Cu map also allowed those precipitates to be clearly observed (Fig. 11e). However, their distribution was not homogeneous. Fig. 12e showed that a diffuse Cu signal was present, but no Cu-rich precipitate was observed in some martensitic laths, whereas in other martensite laths Cu-rich precipitates were clearly detected. Furthermore, Fast Fourier Transform obtained on HRTEM images of a Cu precipitate (previously shown in [33]) allowed to identify a *bcc* crystal structure (a ≈ 3.026 Å and Im$\overline{3}$m space group), which was coherent with the martensite structure.

3.5. Hardness and mechanical properties in traction of CM and AM samples

The differences in microstructure between both AM-H900 and CM-H900 samples were also indirectly analysed by measuring the hardness of the samples. Measurements were also performed for the as-built AM sample and as-received CM sample. The values obtained are presented in Table 2. Considering both macro- and micro-hardness values, the same conclusions could be drawn. The effects of the H900 heat treatment were clearly observed for both the AM and CM samples, with a
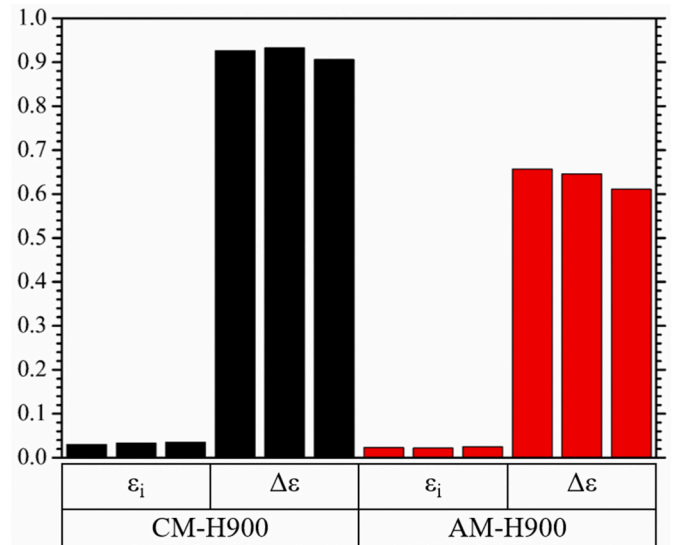
Fig. 15. Comparison of ε_i and $\Delta\varepsilon$ values obtained for AM-H900 and CM-H900 samples.
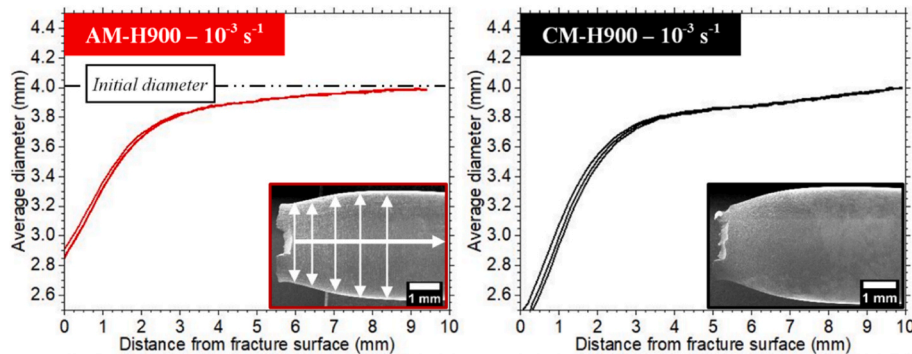

Fig. 14. Evolution of the average diameter of the tensile specimens as a function of the distance from the fracture surface. For each MSS, 3 average curves are displayed, corresponding to 3 tensile specimens; for each tensile specimen, 4 profiles were plotted, so that each value of diameter for a curve is the average of 4 measurements.
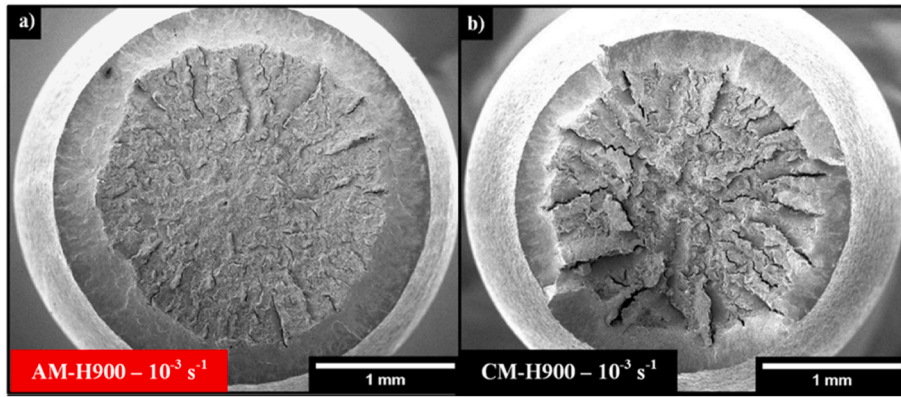
Fig. 16. SEM images of fracture surfaces after tensile tests for a) AM-H900 and b) CM-H900 samples.

significant hardening after H900 heat treatment. The values measured for the CM-H900 sample were slightly higher than those of the AM-H900 sample. Another interesting result was the stronger scattering of the micro-hardness measurements for the AM-H900 sample as compared to the CM-H900 sample.

Fig. 13 shows tensile curves plotted for CM-H900 and AM-H900 samples. The elasticity domain was similar for both MSSs, with the expected value for Young modulus (Table 3). Both MSSs showed similar ultimate tensile strength (UTS) and yield strength ($Rp_{0.2}$) values. Necking was clearly observed for both MSSs. The strain for which necking started was labelled ε_i and was measured when stress started to decrease. Slightly lower values of ε_i were measured for the AM-H900 sample as compared to the CM-H900 sample (Table 3).

To complete the results, the diameter of each tensile specimen was optically measured with a camera all along the gauge length at the end of the tensile tests. The evolutions of the diameter as a function of the distance from the fracture surface are given in Fig. 14. For both MSSs, there was a slow evolution of the diameter of the tensile sample from the severe necking area near the fracture surface to the homogeneously deformed part of the sample where the deformation was ε_i. For the 6 specimens tested, the necking zone was roughly in the centre of the gauge length. Considering the heterogeneity in strain distribution all along the specimen gauge length due to the necking, the strain to fracture, referred to as ε_f, was calculated using the classical assumption of volume conservation during plastic deformation. So, if Φ_0 is the initial diameter of the tensile specimen, and Φ_f is the minimum diameter of the tensile specimen measured close to the fracture surface, then ε_f 2ln (Φ_0/Φ_f). A good repeatability for the strain to fracture ε_f values was observed for both AM-H900 and CM-H900 samples (Table 3). However, ε_f values were significantly higher for CM-H900 sample as compared to AM-H900 sample. Then, $\Delta\varepsilon$ values, defined as $\Delta\varepsilon$ $\varepsilon_f - \varepsilon_i$, were also calculated: $\Delta\varepsilon$ is an indicator of the ductility of the MSSs. Fig. 15 shows $\Delta\varepsilon$ values; ε_i values are also reported. Results showed that $\Delta\varepsilon$ values were significantly lower for AM-H900 samples, as compared to CM-H900 samples, mainly due to the significant differences in ε_f values. Therefore, results showed not only that necking started at slightly smaller strain for AM-H900 samples, but also that AM-H900 MSS was less ductile than the CM-H900 sample. Finally, the true stress to fracture, referred to as σ_R, was calculated as the ratio F_R/S_f, where F_R is the load to fracture, and S_f is the minimum surface section calculated with Φ_f. Significantly higher values of σ_R were obtained for the CM-H900 sample as compared to AM-H900 sample, with a difference of about 300 MPa between the two sets of values.

Fig. 16 shows representative SEM observations of the fracture surfaces after tensile tests. For both MSSs, a global cup and cone ductile fracture, with dimples, was observed overall the surface. Most dimples were associated with NbC precipitates. Both MSSs showed radial cracks following the grain boundaries; they were less numerous and shorter in

the centre of the specimens. The increase in stress triaxiality due to necking induced an increase in hoop stress. Hoop stress values were larger nearby the surface and might explain the radial cracks observed. Considering the larger ε_f values measured for the CM-H900 samples, necking was more severe and might explain deeper cracks for this sample as compared to the AM-H900 sample.

4. Discussion

4.1. Focus on the pores

In an attempt to develop new processes to generate microstructures similar to those obtained with conventional metallurgy, one of the issues related to AM processes could be the presence of gas pores and lack-of-fusion pores in AM parts. However, the results obtained in the current study, with a porosity of about 0.04% only for AM samples, showed that AM processes could lead to a very low porosity for appropriate processing parameters. It was in agreement with work of Hu et al. who showed that they could obtain porosity values in the range [0.025–15] % for scan velocity in the range [10–100] m min^{-1} for 17-4PH powders [2]. Furthermore, as shown in the literature [18,31], the morphology and microstructure of the powder can influence significantly the porosity of the built parts. In powder metallurgy, it is well known that bimodal mixtures improve the density of the produced parts [34]; such a particle size distribution was also reported to be an advantage in the LBM process as it allowed an increase in the overall density of the powder bed and a decrease in porosity phenomenon [18,35]. In the current work, the bimodal distribution of the particle size (Fig. 2) could therefore contribute to explain the very low porosity measured for the AM built parts.

4.2. Austenite/to martensite ratio

As indicated in the introduction, another issue could concern the austenite to martensite ratio which could be significantly different for CM and AM samples even for the same heat treatment. Both XRD (Fig. 8) and energy dispersive XRD analyses performed in the current study confirmed that the microstructure of CM-H900 samples was mostly martensitic (0.8% of austenite only). A nearly-fully martensitic microstructure was also observed for the as-received (2.5% of austenite for H1025) and solution heat treated CM samples. Those results were in good agreement with literature [8,10]. Contrary to the results obtained for the CM-H900 sample, a significant amount of austenite (12.6%) was detected in the AM-H900 samples, as previously shown in the literature [8–13,25,26,29]. Furthermore, the austenite level was estimated to be 12.5% for the as-built AM samples. Those values of the austenite amount should be considered as minimum values since it is known that the austenite to martensite transformation is very sensitive to strain induced

by grinding or polishing [36,37]. Therefore, surface preparation (i.e. polishing) before sample observations could have led to the transformation of some austenite into martensite so that the amount of austenite measured would be lower than what expected. Therefore, the results clearly showed significant differences in the austenite to martensite ratio between AM and CM samples, and it was of interest to try to provide elements of responses to this issue.

Concerning the as-built AM samples, the high amount of austenite could be related to mostly retained austenite untransformed during the quenching following the building process. Nevertheless, the possibility to have a small part of reversed austenite in the thermally affected zone due to the re-melting step could not be neglected. The austenite to martensite ratio in as-built AM samples could be related to the nature of the powder as proposed by various authors [4,6,15,26–28]. In that sense, our result was in good agreement with those of Meredith et al. [28] who showed that non-negligible austenite levels, reaching values as high as 81%, could be measured in the as-built parts for the N_2-atomised powders: this was explained by considering the concentrations of austenite-stabilising elements, e.g. N provided by the atomisation gas, in agreement with recent work of Nezhadfar et al. [25]. In the current study, the austenite amount for as-built AM samples was only 12.5%, which corresponded to a mainly martensitic microstructure, which could be explained by referring to the gas used during the building, in good agreement with Murr et al. work [6] who observed mostly martensitic microstructures for the built parts when the AM process was performed under Ar, independently of the powder. Furthermore, to explain the level of retained austenite in as-built AM samples, Freeman et al. [36] showed that they were able to stabilise a fully austenitic microstructure in an AM 17-4PH MSS at room temperature, because as-built AM 17-4PH MSS contained small solidification cells of 0.2–2 μm that suppressed the thermally-induced martensitic transformation, whereas former austenitic grain size controlled the transformation for wrought MSS [38–43]. Finally, Yadollahi et al. showed that the formation of smaller grains and interdendritic spacing, as well as the presence of strain at high-angle grain boundaries, associated with high dislocation density in AM processes should explain the level of retained austenite in as-built AM samples [12]. Such a stabilisation of austenite was also observed for AM 15-5PH [44].

Then, results of the current study also showed that austenite was no longer detected in the solution heat treated samples (1040 °C for 30 min after the building process), in agreement with literature [8,29]. This could be explained considering that the solution heat treatment at 1040 °C was sufficient to release the internal stresses associated with the AM process, and that thermal stresses induced by the cooling to room temperature after the solution heat treatment were not enough to stabilise austenite. Nezhadfar also proposed that the solution heat treatment at 1040 °C could eliminate the segregation of austenite-stabilising elements resulting from the AM process [25]. However, this hypothesis seemed not to be relevant in the current study because results showed that chemical heterogeneities remained after the solution heat treatment in the AM samples (Fig. 7), probably due to the short duration (i.e. 30 min) at 1040 °C.

The continuing chemical heterogeneities after the solution heat treatment constituted a major result which could contribute to explain the high level of austenite (12.6%) measured after the ageing at 480 °C in the AM samples (AM-H900 samples), whereas only 0.8% of austenite was detected for the CM-H900 samples. STEM observations showed that austenite was present in AM-H900 sample, both as retained austenite grains localised between two martensite laths belonging to the same packet (Fig. 11), and as a thin layer of reversed austenite wrapping up a martensite lath (Fig. 12). Considering that no retained austenite was detected in the AM solution heat treated samples, results clearly showed that most part of the austenite phase observed in AM-H900 samples formed during the ageing at 480 °C, which means that most part of the austenite present in the AM-H900 samples was reversed austenite. Kapoor and Batra [45] studied the martensite to austenite

transformation with different continuous heating rates in a dilatometer for a 17-4PH CM MSS. They observed that the martensite to austenite transformation started from 650 °C for the lowest heating rate studied, i. e. 0.032 °C s^{-1}. Considering the heating rate (5 °C/min) used during the H900 ageing in the current study, very little martensite should reverse to austenite during the ageing, which was in agreement with the diffractogram obtained for the CM-H900 sample (Fig. 8). However, such a transformation was likely to occur more easily in the presence of localised chemical heterogeneities [26], and, as previously said, Fig. 7 clearly showed the heterogeneous distribution in alloying elements in the AM solution heat treated sample. Furthermore, Fig. 9 demonstrated that this specific distribution of the alloying elements in the AM solution heat treated samples was associated with a decrease in the Ms value as compared to the CM solution heat treated sample. With the hypothesis that the starting temperature of martensite to austenite transformation was the same for both solution heat treated AM and CM samples, this meant that the driving force associated with the transformation was higher for the solution heat treated AM sample, which should promote the formation of reversed austenite during the ageing at 480 °C for AM samples.

Finally, other microstructural features should explain the high amount of reversed austenite in the AM-H900 samples. TEM observations (Fig. 10) showed that AM-H900 samples had finer martensite laths than CM-H900 samples, which has been already mentioned in the literature [25,46]. This difference in lath size was also true for the solution heat treated samples because the ageing at 480 °C was not expected to modify the lath size. No definite explanations could be found in the literature to explain such a difference. The prior austenite grain size, C content, and dislocation density were often cited to have a significant effect on the size of the martensite lath packets [47,48]. Moreover, we showed in a previous study that Si-rich inclusions were observed in AM samples [33], as well as carbides (Fig. 5d). Those inclusions and precipitates might induce finer microstructures [8]. Considering that the interfaces between the martensite laths constituted nucleation sites for reversed austenite, a decrease in the lath size meant an increase in the density of nucleation sites. Furthermore, as the growth rate for reversed austenite nuclei was controlled by diffusion processes of austenite-stabilising elements at the interfaces between the martensite laths, a finer microstructure should accelerate the growth of those nuclei, which could contribute to explain also the high amount of reversed austenite in the AM-H900 sample.

4.3. Cu-rich precipitates

Nevertheless, it is well-known that the ageing at 480 °C is also associated with the formation of Cu-rich precipitates [2,25,29,49,50]. In the current study, significant differences were also observed between AM and CM samples concerning the Cu-rich precipitation. STEM observations (Figs. 11 and 12) showed a higher density of Cu-rich precipitates in the AM-H900 sample as compared to the CM-H900 sample, which could be explained by smaller precipitates in the CM-H900 samples as compared to AM-H900 sample. Indeed, detailed analysis of those precipitates for the AM-H900 samples showed that they were coarser, i.e. 10–15 nm, than expected for a H900 heat treatment, i.e. 4–5 nm [8,51]. Moreover, Lee et al. [52] showed that, under a critical size of 4 nm in diameter, Cu-rich precipitates were bcc clusters, coherent with the martensite structure. But, when Cu-rich precipitates grew, they underwent a martensitic transformation leading first to a 9 R crystal lattice structure (twinned orthorhombic structure), and then to a 3 R lattice structure that evolved continuously to a stress relaxed fcc lattice [53–55]. Therefore, it was surprising to observe in the current study, not only such large Cu-rich precipitates for a H900 heat treatment, but also a bcc structure for 10 nm in diameter Cu-rich precipitates. All the specific microstructural features previously cited for the AM-H900 samples could contribute to explain these observations. It could be assumed that finer martensite laths were associated with a higher level of internal

stresses that could impact the critical solubility limit of Cu in the martensite lattice, and therefore had a significant influence on both the germination and growth of Cu-rich precipitates. Consequently, depending on the level of internal stresses in the martensite laths, Cu-rich precipitates could form or not, which could explain the heterogeneity in the distribution of Cu-rich precipitates for the AM-H900 sample. Furthermore, the internal stresses could also stabilise the bcc structure, so that it was observed for a precipitate size significantly higher than that expected for such a crystallographic structure.

4.4. Microstructural singularities of AM 17-4PH and mechanical properties

The discussion proposed in the three previous paragraphs clearly showed significant differences in the microstructure between the AM-H900 and CM-H900 samples. However, the effect of the microstructure on the mechanical properties of the MSSs had to be considered as the overall contribution of different microstructural parameters: Cu-rich precipitates and austenite to martensite ratio, as well as the size and distribution of martensite laths, the density and size of inclusions and carbides. The deconvolution of each individual contribution was not trivial.

Concerning hardness measurements, the higher amount of reversed austenite in the AM-H900 sample as compared to the CM-H900 sample could contribute to explain the lower hardness measured for AM-H900 samples [26]. However, the influence of Cu precipitates could not be neglected; indeed, literature data showed that these precipitates contribute significantly to the hardening of this steel [2,25,29,49,50]. Therefore, differences in hardness between the AM-H900 and CM-H900 samples could be also related to subtle differences in the Cu-rich precipitates as suggested by Sun et al. [8]. The differences in size observed in the current study, with coarser Cu-rich precipitates in the AM-H900 samples, could therefore contribute to the decrease in hardness observed for the AM-H900 sample as compared to the CM-H900 sample. Finally, the scattering in the hardness values shown for the AM-H900 sample could be associated with the heterogeneous distribution of both reversed austenite and Cu-rich precipitates.

Another major result of the current study was that, despite noticeable microstructural differences, surprisingly, AM-H900 and CM-H900 samples showed quite similar tensile behaviour at room temperature, with similar UTS and $Rp_{0.2}$ values, in agreement with Sun et al. [8]. However, some subtle differences were seen and, first, attention was paid to the pores to explain the results. In the literature, authors reported that pores lead to poor repeatability and a decrease in the elongation to fracture [20,29,56–61]. In the current study, the good repeatability in the strain to fracture values for the AM-H900 samples was in agreement with the low porosity pointed out previously. Such a low amount of pores in the AM built parts was also in good agreement with the Young modulus values (Table 3) measured from the tensile curves (Fig. 13), with similar values for both CM-H900 and AM-H900 samples. However, the decrease in the ε_f and $\Delta\varepsilon$ values for AM-H900 samples (Table 3), as compared to CM-H900 samples, led us to assume that, for high level of stress, the influence of pores could not be neglected. Indeed, the higher amount of reversed austenite measured for the AM-H900 sample should have increased its ductility [29] contrary to what was observed. This showed that the influence of the austenite to martensite ratio was counterbalanced by the effect of other microstructural features, i.e. pores, as previously said, but also NbC, which could contribute also to the ductility loss of AM-H900. As illustrated in Fig. 14, necking was more pronounced for the CM-H900 sample increasing local stress triaxiality, and therefore local stresses including hoop stress because fewer sites (NbC carbides and inclusions) were available to initiate cavitation by comparison to the AM-H900 samples. The stress field was less and less homogenous in the cross-section as this section decreased. Such a stress field, in synergy with the smaller number of cavitation initiation sites, led to higher stresses associated with fracture initiation, for the CM-H900 samples.

5. Conclusions

This manuscript aimed to analyse the microstructure of a 17–4PH martensitic stainless steel (MSS) produced by additive manufacturing (AM), with laser beam melting process, by comparison to conventional metallurgy (CM). Both materials were in the same heat treatment state, i.e. H900 heat treatment, which consisted of an annealing at 1040 °C followed by an ageing treatment at 480 °C. The main conclusions were the following:

1. At the OM scale, no significant difference was observed between the two MSSs with, for both MSSs, a globally martensitic microstructure and similar grain size, but more numerous intergranular carbides for the AM-H900 sample.

2. However, XRD analysis showed a significantly higher austenite content, i.e. 12.6% for the AM-H900 sample, as compared to the CM-H900 sample (0.8%). Additional TEM and STEM studies showed that both reversed and retained austenite was present in the AM-H900 sample. Furthermore, TEM observations also showed that i) the martensite laths were wider for the CM-H900 sample as compared to the AM-H900 sample; ii) Cu-rich precipitates were more numerous and bigger in AM-H900 samples, with a 10 to 15-nm diameter three times larger than expected for the H900 ageing treatment.

3. The high amount of reversed austenite detected in the AM-H900 sample was explained by a heterogeneous distribution of austenite-stabilising alloying elements clearly observed by SEM-EDS after the solution heat treatment at 1040 °C. Such a microstructural feature was suspected to be the major reason for the decrease in Ms value measured for the solution heat treated AM sample, as compared to the solution heat treated CM sample. This was associated with an increase in the driving force for the martensite to austenite transformation during the ageing at 480 °C. Furthermore, the finer martensite lath size observed for the AM sample as compared to the CM sample was interpreted as an increase in reversed austenite nucleation sites, and promoted also the diffusion-controlled growth of this last phase by accelerating the diffusion of austenite-stabilising elements at the interface between martensite laths.

4. Despite significant differences in microstructures, both AM-H900 and CM-H900 MSSs showed similar tensile properties, with quite similar UTS and $Rp_{0.2}$ values. Nevertheless, the AM-H900 sample was found to be less ductile as compared to CM-H900 sample, which could be attributed, at least partially, to the pores and NbC present in the AM samples, and even though the porosity was found to be very low.

Therefore, the results obtained in the current study clearly showed that 17-4PH MSS obtained through additive manufacturing was a promising candidate for parts used at room temperature under tensile conditions. Nevertheless, it was of major interest to keep in mind that the differences in microstructures shown between AM-H900 and CM-H900 samples should generate changes in some in-service properties, e.g. the corrosion behavior and/or stress corrosion cracking behavior. Literature data exist on this topic, but this issue deserves to be studied more extensively.

Data availability

The raw/processed data required to reproduce these findings cannot be shared at this time as the data also forms part of an ongoing study.

Declaration of competing interest

The authors declare that they have no known competing financial interests or personal relationships that could have appeared to influence the work reported in this paper.

References

[1] A. Yadollahi, N. Shamsaei, S.M. Thompson, A. Elwany, L. Bian, Effects of building orientation and heat treatment on fatigue behavior of selective laser melted 17-4 PH stainless steel, Int. J. Fatig. 94 (2) (2017) 218–235, https://doi.org/10.1016/j.ijfatigue.2016.03.014.

[2] Z. Hu, H. Zhu, H. Zhang, X. Zeng, Experimental investigation on selective laser melting of 17-4PH stainless steel, Opt Laser. Technol. 87 (2017) 17–25, https://doi.org/10.1016/j.optlastec.2016.07.012.

[3] M. Mahmoudi, A. Elwany, A. Yadollahi, S.- M Thompson, L.-K. Bian, N. Shamsaei, Mechanical properties and microstructural characterization of selective laser melted 17-4 PH stainless steel, Rapid Prototyp. J. 23 (2017) 280–294, https://doi.org/10.1108/RPJ-12-2015-0192.

[4] S. Pasebani, M. Ghayoor, S. Badwe, H. Irrinki, S.V. Atre, Effects of atomizing media and post processing on mechanical properties of 17-4 PH stainless steel manufactured via selective laser melting, Addit. Manuf. 22 (2018) 127–137, https://doi.org/10.1016/j.addma.2018.05.011.

[5] R. Rashid, S.H. Masood, D. Ruan, S. Palanisamy, R.A. Rahman Rashid, M. Brandt, Effect of scan strategy on density and metallurgical properties of 17-4PH parts printed by selective laser melting (SLM), J. Mater. Process. Technol. 249 (2017) 502–511, https://doi.org/10.1016/j.jmatprotec.2017.06.023.

[6] L.E. Murr, E. Martinez, J. Hernandez, S. Collins, K.N. Amato, S.M. Gaytan, P. W. Shindo, Microstructures and properties of 17-4 PH stainless steel fabricated by selective laser melting, J. Mater. Res. Technol. 1 (2012) 167–177, https://doi.org/10.1016/S2238-7854(12)70029-7.

[7] H.K. Rafi, D. Pal, N. Patil, T.L. Starr, B.E. Stucker, Microstructure and mechanical behavior of 17-4 precipitation hardenable steel processed by selective laser melting, J. Mater. Eng. Perform. 23 (2014) 4421–4428, https://doi.org/10.1007/s11665-014-1226-y.

[8] Y. Sun, R.J. Hebert, M. Aindow, Effect of heat treatments on microstructural evolution of additively manufactured and wrought 17-4PH stainless steel, Mater. Des. 156 (2018) 429–440, https://doi.org/10.1016/j.matdes.2018.07.015.

[9] P.D. Nezhadfar, E. Burford, K. Anderson-Wedge, B. Zhang, S. Shao, S.R. Daniewicz, N. Shamsaei, Fatigue crack growth behavior of additively manufactured 17-4 PH stainless steel: effects of build orientation and microstructure, Intern. J. fatigue. 123 (2019) 168–179, https://doi.org/10.1016/j.ijfatigue.2019.02.015.

[10] S. Cheruvathur, E.-A. Lass, C.-E. Campbell, Additive manufacturing of 17-4 PH stainless steel: post-processing heat treatment to achieve uniform reproducible microstructure, J. Miner. Met. Mater. Soc. 68 (2016) 930–942, https://doi.org/10.1007/s11837-015-1754-4.

[11] Y. Sun, R.J. Hebert, M. Aindow, Effect of laser scan length on the microstructure of additively manufactured 17-4PH stainless steel thin-walled parts, Addit. Manuf. 35 (2020) 101302, https://doi.org/10.1016/j.addma.2020.101302.

[12] A. Yadollahi, M. Mahmoudi, A. Elwany, H. Doude, L. Bian, J.C. Newman, Effects of crack orientation and heat treatment on fatigue-crack-growth behavior of AM 17-4 PH stainless steel, Eng. Fract. Mech. 226 (2020) 106874, https://doi.org/10.1016/j.engfracmech.2020.106874.

[13] P. Leo, S. D'Ostuni, P. Perulli, M.A.C. Sastre, A.I. Fernández-Abia, J. Barreiro, Analysis of microstructure and defects in 17-4 PH stainless steel sample manufactured by Selective Laser Melting, Procedia Manuf 41 (2019) 66–73, https://doi.org/10.1016/j.promfg.2019.07.030.

[14] D. Herzog, V. Seyda, E. Wycisk, C. Emmelmann, Additive manufacturing of metals, Acta Mater. 117 (2016) 371–392, https://doi.org/10.1016/j.actamat.2016.07.019.

[15] S. Vunnam, A. Saboo, C. Sudbrack, T.L. Starr, Effect of powder chemical composition on the as-built microstructure of 17-4 PH stainless steel processed by selective laser melting, Add. Manufact. 30 (2019) 100876, https://doi.org/10.1016/j.addma.2019.100876.

[16] A.B. Spierings, M. Schneider, R. Eggenberger, Comparison of density measurement techniques for additive manufactured metallic parts, Rapid Prototyp. J. 17 (2011) 380–386, https://doi.org/10.1108/13552541111156504.

[17] A. Sola, A. Nouri, Microstructural porosity in additive manufacturing: the formation and detection of pores in metal parts fabricated by powder bed fusion, J. Advanc. Manufact. Process. 1 (2019), e10021, https://doi.org/10.1002/amp2.10021.

[18] H. Irrinki, J.S.D. Jangam, S. Pasebani, S. Badwe, J. Stitzel, K. Kate, O. Gulsoy, S. V. Atre, Effects of particle characteristics on the microstructure and mechanical properties of 17-4 PH stainless steel fabricated by laser-powder bed fusion, Powder Technol. 331 (2018) 192–203, https://doi.org/10.1016/j.powtec.2018.03.025.

[19] J.A. Cherry, H.M. Davies, S. Mehmood, N.P. Lavery, S.G.R. Brown, J. Sienz, Investigation into the effect of process parameters on microstructural and physical properties of 316L stainless steel parts by selective laser melting, Int. J. Adv.

[20] U. Ali, R. Esmaeilizadeh, F. Ahmed, D. Sarker, W. Muhammad, A. Keshavarzkermani, Y. Mahmoodkhani, E. Marzbanrad, E. Toyserkani, Identification and characterization of spatter particles and their effect on surface roughness, density and mechanical response of 17-4 PH stainless steel laser powder-bed fusion parts, Mater. Sci. Eng. 756 (2019) 98–107, https://doi.org/10.1016/j.msea.2019.04.026.

[21] O.K. Von Goldbeck, Iron—copper Fe—Cu, in: IRON—Binary Phase Diagrams, Springer Berlin Heidelberg, 1982, pp. 35–37, https://doi.org/10.1007/978-3-662-08024-5_18.

[22] C.N. Hsiao, C.S. Chiou, J.R. Yang, Aging reactions in a 17-4 PH stainless steel, Mater. Chem. Phys. 74 (2002) 134–142, https://doi.org/10.1016/S0254-0584(01)00460-6.

[23] M. Alnajjar, F. Christien, K. Wolski, C. Bosch, Evidence of austenite by-passing in a stainless steel obtained from laser melting additive manufacturing, Add. Manuf. 25 (2019) 187–195, https://doi.org/10.1016/j.addma.2018.11.004.

[24] M. Alnajjar, F. Christien, C. Bosch, K. Wolski, A comparative study of microstructure and hydrogen embrittlement of selective laser melted and wrought 17–4 PH stainless steel, Mater. Sci. Eng. 785 (2020), https://doi.org/10.1016/j.msea.2020.139363.

[25] P.D. Nezhadfar, R. Shrestha, N. Phan, N. Shamsaei, Fatigue behavior of additively manufactured 17-4 PH stainless steel: synergistic effects of surface roughness and heat treatment, Int. J. Fatig. 124 (2019) 188–204, https://doi.org/10.1016/j.ijfatigue.2019.02.039.

[26] D. Wang, C.T. Chi, W.Q. Wang, Y.L. Li, M.S. Wang, X.G. Chen, Z.H. Chen, X. P. Cheng, Y.J. Xie, The effects of fabrication atmosphere condition on the microstructural and mechanical properties of laser direct manufactured stainless steel 17-4 PH, J. Mater. Sci. Technol. 35 (2019) 1315–1322, https://doi.org/10.1016/j.jmst.2019.03.009.

[27] P. Zapico, S. Giganto, J. Barreiro, S. Martínez-Pellitero, Characterisation of 17-4PH metallic powder recycling to optimise the performance of the selective laser melting process, J. Mater. Res. Technol. 9 (2020) 1273–1285, https://doi.org/10.1016/j.jmrt.2019.11.054.

[28] S.D. Meredith, J.S. Zuback, J.S. Keist, T.A. Palmer, Impact of composition on the heat treatment response of additively manufactured 17–4 PH grade stainless steel, Mater. Sci. Eng. 738 (2018) 44–56, https://doi.org/10.1016/J.MSEA.2018.09.066.

[29] T. LeBrun, T. Nakamoto, K. Horikawa, H. Kobayashi, Effect of retained austenite on subsequent thermal processing and resultant mechanical properties of selective laser melted 17–4 PH stainless steel, Mater. Des. 81 (2015) 44–53, https://doi.org/10.1016/j.matdes.2015.05.026.

[30] ASTM E112-13, Standard Test Methods for Determining Average Grain Size, ASTM International, West Conshohocken, PA, 2013, https://doi.org/10.1520/E0112-13. www.astm.org.

[31] F. Ahmed, U. Ali, D. Sarker, E. Marzbanrad, K. Choi, Y. Mahmoodkhani, E. Toyserkani, Study of powder recycling and its effect on printed parts during laser powder-bed fusion of 17-4 PH stainless steel, J. Mater. Process. Technol. 278 (2020) 116522, https://doi.org/10.1016/j.jmatprotec.2019.116522.

[32] W. Hou, Q. Liu, J. Gu, Nano-sized austenite and Cu precipitates formed by using intercritical tempering plus tempering and their effect on the mechanical property in a low carbon Cu bearing 7 Ni steel, Mater. Sci. Eng. 780 (2020) 139186, https://doi.org/10.1016/j.msea.2020.139186.

[33] A. Barroux, N. Ducommun, E. Nivet, L. Laffont, C. Blanc, Pitting corrosion of 17-4PH stainless steel manufactured by laser beam melting, Corrosion Sci. 169 (2020) 108594, https://doi.org/10.1016/j.corsci.2020.108594. Article.

[34] A. Bose, Chapter 1 - introduction to particulate materials, in: A. Bose (Ed.), Advances in Particulate Materials, Butterworth-Heinemann, Boston, 1995, pp. 1–52, https://doi.org/10.1016/B978-0-7506-9156-7.50006-9.

[35] S.E. Brika, M. Letenneur, C.A. Dion, V. Brailovski, Influence of particle morphology and size distribution on the powder flowability and laser powder bed fusion manufacturability of Ti-6Al-4V alloy, Add. Manuf. 31 (2020) 100929, https://doi.org/10.1016/j.addma.2019.100929.

[36] F.S.H.B. Freeman, J. Sharp, J. Xi, I. Todd, Influence of solidification cell structure on the martensitic transformation in additively manufactured steels, Addit. Manuf. 30 (2019) 100917, https://doi.org/10.1016/j.addma.2019.100917.

[37] L. Facchini, N. Vicente, I. Lonardelli, E. Magalini, P. Robotti, A. Molinari, Metastable Austenite in 17–4 precipitation-hardening stainless steel produced by selective laser melting, Adv. Eng. Mater. 12 (2010) 184–188, https://doi.org/10.1002/adem.200900259.

[38] S. Takaki, K. Fukunaga, J. Syarif, T. Tsuchiyama, Effect of grain refinement on thermal stability of metastable Austenitic steel, Mater. Trans. 45 (2004) 2245–2251, https://doi.org/10.2320/matertrans.45.2245.

[39] H.-S. Yang, H.K.D.H. Bhadeshia, Austenite grain size and the martensite-start temperature, Scripta Mater. 60 (2009) 493–495, https://doi.org/10.1016/j.scriptamat.2008.11.043.

[40] J.R.C. Guimaraes, P.R. Rios, Martensite start temperature and the austenite grain-size, J. Mater. Sci. 45 (2010) 1074–1077, https://doi.org/10.1007/s10853-009-4044-0.

[41] T. Hanamura, S. Torizuka, S. Tamura, S. Enokida, H. Takechi, Effect of austenite grain size on transformation behavior, microstructure and mechanical properties of 0.1C–5Mn martensitic steel, ISIJ Int. 53 (2013) 2218–2225, https://doi.org/10.2355/isijinternational.53.2218.

[42] J. Hidalgo, M.J. Santofimia, Effect of prior austenite grain size refinement by thermal cycling on the microstructural features of as-quenched lath martensite, Metall. Mater. Trans. 47 (2016) 5288–5301, https://doi.org/10.1007/s11661-016-3525-4.

Manuf. Technol. 76 (2015) 869–879, https://doi.org/10.1007/s00170-014-6297-2.

[43] C. Celada Casero, J. Sietsma, M.J. Santofimia, The role of the austenite grain size in the martensitic transformation in low carbon steels, Mater. Des. 167 (2019) 107625, https://doi.org/10.1016/j.matdes.2019.107625.

[44] X.D. Nong, X.L. Zhou, J.H. Li, Y.D. Wang, Y.F. Zhao, M. Brochu, Selective laser melting and heat treatment of precipitation hardening stainless steel with a refined microstructure and excellent mechanical properties, Scripta Mater. 178 (2020) 7–12, https://doi.org/10.1016/j.scriptamat.2019.10.040.

[45] R. Kapoor, I.S. Batra, On the α' to γ transformation in maraging (grade 350), PH 13-8 Mo and 17-4 PH steels, Mat, Sci. Eng. A. 371 (2004) 324–334, https://doi.org/10.1016/j.msea.2003.12.023.

[46] T.H. Hsu, Y.J. Chang, C.Y. Huang, H.W. Yen, C.P. Chen, K.K. Jen, A.C. Yeh, Microstructure and property of a selective laser melting process induced oxide dispersion strengthened 17-4 PH stainless steel, J. Alloys Compd. 803 (2019) 30–41, https://doi.org/10.1016/j.jallcom.2019.06.289.

[47] T. Maki, 2 - morphology and substructure of martensite in steels, in: E. Pereloma, D.V. Edmonds (Eds.), Phase Transformations in Steels, Woodhead Publishing, 2012, pp. 34–58, https://doi.org/10.1533/9780857096111.1.34.

[48] T. Swarr, G. Krauss, The effect of structure on the deformation of as-quenched and tempered martensite in an Fe-0.2 pct C alloy, Metal. Trans. A. 7 (1976) 41–48, https://doi.org/10.1007/BF02644037.

[49] C.Y. Chung, Y.C. Tzeng, Effects of aging treatment on the precipitation behavior of ε-Cu phase and mechanical properties of metal injection molding 17-4PH stainless steel, Mater. Lett. 237 (2019) 228–231, https://doi.org/10.1016/j.matlet.2018.11.107.

[50] H. Mirzadeh, A. Najafizadeh, Aging kinetics of 17-4 PH stainless steel, Mater. Chem. Phys. 116 (2009) 119–124, https://doi.org/10.1016/j.matchemphys.2009.02.049.

[51] G. Yeli, M.A. Auger, K. Wilford, G.D.W. Smith, P.A.J. Bagot, M.P. Moody, Sequential nucleation of phases in a 17-4PH steel: microstructural characterisation and mechanical properties, Acta Mater. 125 (2017) 38–49, https://doi.org/10.1016/j.actamat.2016.11.052.

[52] T.-H. Lee, Y.-O. Kim, S.-J. Kim, Crystallographic model for bcc-to-9R martensitic transformation of Cu precipitates in ferritic steel, Phil. Mag. 87 (2007) 209–224, https://doi.org/10.1080/14786430600909014.

[53] Y. Le Bouar, Atomistic study of the coherency loss during the B.C.C.–9R transformation of small copper precipitates in ferritic steels, Acta Mater. 49 (2001) 2661–2669, https://doi.org/10.1016/S1359-6454(01)00178-1.

[54] J.-H. Wu, C.-K. Lin, Influence of high temperature exposure on the mechanical behavior and microstructure of 17-4 PH stainless steel, J. Mat. Sci. 38 (2003) 965–971, https://doi.org/10.1023/A:1022377225704.

[55] M. Murayama, K. Hono, Y. Katayama, Microstructural evolution in a 17-4 PH stainless steel after aging at 400 °C, Metall. Mater. Trans. 30 (1999) 345–353, https://doi.org/10.1007/s11661-999-0323-2.

[56] L. Carneiro, B. Jalalahmadi, A. Ashtekar, Y. Jiang, Cyclic deformation and fatigue behavior of additively manufactured 17–4 PH stainless steel, Int. J. Fatig. 123 (2019) 22–30, https://doi.org/10.1016/j.ijfatigue.2019.02.006.

[57] A.D. Dressler, E.W. Jost, J.C. Miers, D.G. Moore, C.C. Seepersad, B.L. Boyce, Heterogeneities dominate mechanical performance of additively manufactured metal lattice struts, Add. Manuf. 28 (2019) 692–703, https://doi.org/10.1016/j.addma.2019.06.011.

[58] N. Vanderesse, D. Texier, P. Bocher, Effect of porosities on brazed martensitic steel tensile properties: 2D and 3D pre-mortem vs post-mortem characterizations, Mater. Char. 160 (2020) 110084, https://doi.org/10.1016/j.matchar.2019.110084.

[59] J. Gonzalez-Gutierrez, F. Arbeiter, T. Schlauf, C. Kukla, C. Holzer, Tensile properties of sintered 17-4PH stainless steel fabricated by material extrusion additive manufacturing, Mater. Lett. 248 (2019) 165–168, https://doi.org/10.1016/j.matlet.2019.04.024.

[60] F. Huber, C. Bischof, O. Hentschel, J. Heberle, J. Zettl, K.Yu Nagulin, M. Schmidt, Laser beam melting and heat-treatment of 1.2343 (AISI H11) tool steel – microstructure and mechanical properties, Mater. Sci. Eng. 742 (2019) 109–115, https://doi.org/10.1016/j.msea.2018.11.001.

[61] T. Lebrun, K. Tanigaki, K. Horikawa, H. Kobayashi, Strain rate sensitivity and mechanical anisotropy of selective laser melted 17-4 PH stainless steel, Mech. Eng. J. 1 (2014), https://doi.org/10.1299/MEJ.2014SMM0049. UNSP 14-00274.